Methods for evaluating geometric distortion in magnetic resonance imaging

Ville Isokoski

M.Sc. thesis
Physics degree programme
University of Oulu
2021

Abstract

Geometric distortions and spatial inaccuracies in magnetic resonance imaging are an important concern especially in image-guided high accuracy operations, such as radiotherapy or stereotactic surgeries. Geometric distortions in the images are in principle caused by erroneous spatial encoding of the signal echo. Errors in the spatial encoding are caused by different physical factors, such as static field inhomogeneity, gradient field nonlinearities, chemical shift, and magnetic susceptibility. The distortion shifts can be quantitatively evaluated as the amount of distance or pixels that a signal source has shifted in the mapping from real space to the image space. By studying the distortions and the causing mechanisms, corrective measures can be taken to minimize spatial errors in the images.

In this thesis the geometric distortions of one MRI scanner are evaluated with four different grid phantom objects. The scanner was a 3 Tesla scanner at the Oulu University Hospital. The phantoms included two commercial readily available MRI quality assurance phantoms and two in-house produced prototype phantoms. The methods consisted of imaging the phantoms with different two- and three-dimensional sequences. Image and distortion analysis was performed with one commercial distortion check software for the respective commercial phantom, and with an in-house developed Matlab program for all four phantoms.

Results for the magnitude and direction of the distortion as a function of distance from the scanner isocenter were acquired. Three-dimensional distortion shifts up 4 mm within a radius of 200 mm from the isocenter were measured, with occasional shifts up to 9 mm between 100 and 200 mm from the isocenter. Distortion field maps and contour plots produced with both analysis methods seemed to be in accordance with each other, and the geometry and behaviour of the field was found to be as expected. As to the prototype phantoms, a result with respect to the grid density was found. A 5 mm grid separation was too dense with respect to the achievable resolution for the Matlab analysis script to function, or more generally for any distortion check at all.

Tiivistelmä

Magneettikuvien geometriset vääristymät ja epätarkkuudet ovat tärkeitä huomioon otettavia asioita erityisesti sädehoitoihin tai kirurgisiin operaatioihin liittyvissä kuvantamisissa. Kuvien vääristymät aiheutuvat virheistä signaalien paikkakoodauksessa. Paikkakoodaukseen aiheutuu virheitä eri fysikaalisista tekijöistä, kuten staattisen magneettikentän epähomogeenisuuksista, gradienttikenttien epälineaarisuuksista, kemiallisesta siirtymästä tai magneettisesta suskeptibiliteetistä. Geometrinen vääristymä voidaan määrittää kvantitatiivisesti tutkimalla signaalin paikan siirtymää kuvauksessa todellisesta koordinaatistosta, eli kuvattavasta kohteesta, kuvan koordinaatistoon. Kuvia voidaan myös korjata vääristymien osalta tutkimalla vääristymien luonnetta ja niiden aiheuttajia.

Tässä tutkielmassa tutkittiin Oulun yliopistollisen sairaalan yhden 3 Teslan kenttävoimakkuuden magneettikuvauslaitteen geometrista vääristymää. Kuvauksissa käytettiin neljää erilaista fantomia, kahta valmista kaupallisesti saatavilla olevaa sekä kahta kokeellista prototyyppiä. Fantomeita kuvattiin eri kaksi- ja kolmiulotteisilla kuvaussekvensseillä. Kuva- ja vääristymäanalyysiä varten käytettiin yhtä kaupallista ohjelmaa, joka on tarkoitettu sitä vastaavalle fantomille, sekä itse sairaalassa kehitettyä Matlab-pohjaista ohjelmaa.

Mittausten perusteella saatiin kvantitatiiviset tulokset vääristymän suuruudelle ja suunnalle, etäisyyden funktiona skannerin keskipisteestä. Kolmiulotteisten vääristymien suuruudet olivat 4 mm tai alle 200 mm säteelle asti, suurimpien yksittäisten vääristymien ollessa noin 9 mm tai alle 100 mm ja 200 mm etäisyyksien välillä. Molemmilla analyysiohjelmilla vääristymien suuntien perusteella luodut vektorikentät olivat toistensa mukaisia ja vääristymän käyttäytyminen vaikutti odotetulta. Prototyyppifantomien suhteen päädyttiin tulokseen, jonka mukaan 5 mm ruudukko oli liian tiheä suhteessa resoluutioon, eikä Matlab-pohjainen analyysi toiminut. Tarpeeksi leveä ruudukko oli siten oleellinen osa vääristymän määrittämistä.

Abbreviations

2D	Two-dimensional
3D	Three-dimensional
ACR	American College of Radiology
CIRS	Computerized Imaging Reference Systems, Inc.
CT	Computed tomography
DBS	Deep brain stimulation
FID	Free induction decay
FOV	Field of view
FT	Fourier transform
GE	Gradient echo
GTV	Gross tumor volume
IR	Inversion recovery
MRI	Magnetic resonance imaging
NMR	Nuclear magnetic resonance
RF	Radio frequency
RMS	Root mean square
SE	Spin echo
SNR	Signal-to-noise ratio
SRS	Stereotactic radiosurgery
TE	Time to echo
TR	Time to repetition

Symbols

B_0	Static magnetic field flux density
B_1	Radio frequency magnetic field flux density
G_{FE}/G_R	Frequency encoding/readout gradient
G_{PE}	Phase encoding gradient
$G_{x,y,z}$	Gradient in the x, y or z direction
H	Magnetic field strength
$\hbar$	Dirac constant
k	Spatial frequency
k_B	Boltzmann constant
M_0	Equilibrium magnetization
$M_{x,y,z}$	Magnetization in the x, y, or z direction
$M_\perp$	Transverse magnetization
T	Temperature
t	Time
γ	Gyromagnetic ratio
χ	Magnetic susceptibility
ω_0	Larmor frequency

Contents

Chapter 1

Introduction

Geometric distortion in magnetic resonance imaging (MRI) became a subject of interest quickly after the development of first MRI scanners in the 1970s. Due to the indirect nature of image formation and spatial encoding of the signal, spatial inaccuracies and distortions, among other artifacts, are always present. The spatial or geometrical accuracy in MRI is of particular concern when the images are used in planning for operations demanding high accuracy. Arising from some hardware related sources, such as inhomogeneity of the static and nonlinearity of the gradient magnetic fields, as well as from the object or patient being imaged, some geometric inaccuracies in the image are inevitable. Although not always relevant in basic diagnostics, distortions even in the order of millimeters can lead to difficulties and unnecessary damage in brain surgeries. One example of such surgery is the electrode implantation for deep brain stimulation (DBS) in Parkinson's disease treatment [1, 2]. Likewise in radiotherapy planning, geometric distortions have a direct and considerable dosimetric impact, depending on the object size [3, 4].

A growing interest in the geometrical accuracy of MRI can be seen in the increasing amount of studies performed annually. For example, studies comparing different scanners, field strengths, and pulse sequences have been made (*e.g.* [5, 6]). Although new methods and phantoms for evaluating the distortions have been introduced, there is no widely accepted standard for the amount of distortion acceptable or for the methods to evaluate it, not yet at least. If a practical limit for the acceptable amount of spatial uncertainty in the images is needed, the accuracy limits concerning, for example, fusion of MRI images with computed tomography (CT) images for radiotherapy planning can be taken as a reference.

The evaluation of geometrical accuracy has been a part of the quality assurance programs for some time, but they often lack the proper quantitative methods and criteria, leaving room for improvement. Also, the distortion correction methods provided by the scanner manufacturer, such as passive and active shimming of the static field or algorithms in the reconstruction software, which provide some two-dimensional (2D) or three-dimensional (3D) distortion correction, succeed in reducing the geometric distortions. However, as not all sources of distortion can be taken into account quantitatively, some residual error still remains. It can be said that the task at hand has been concentrated in minimizing the distortions and developing suitable qualitative and quantitative methods for routine quality assurance and further studies. [7, 8]

This thesis was done at the Oulu University Hospital with an aim of evaluating the residual geometric distortion of selected scanners quantitatively. This included the purpose of testing and validating a new 3D printed grid phantom. However, somewhat unexpected intermediate results concerning the grid density led to a more methodological approach. Now, the structure of this thesis consists of a brief look at the background surrounding the subject, followed by methodological testing and quantitative evaluation of the geometric distortion of one 3 T scanner, an essential scanner used for high-accuracy operations planning. The materials and methods used consist of two readily available commercial phantoms and two in-house 3D printed prototype phantoms, along with a commercial distortion check program and an early stage in-house developed Matlab program. Finally, the results for all phantoms are discussed comparatively. Some conclusions about the effect of grid density and the structure of the phantoms are made, along with comparison of methodological superiority.

Chapter 2

Background

In order to gain an understanding of geometric distortion in MRI, it is necessary to establish an overview of the basic principles of MRI and the causing mechanisms of distortion in the images. In this chapter, the basics of image formation from nuclear magnetic resonance (NMR) with spatial signal encoding are introduced and the principle causes of distortion are discussed. Adding to the introductory chapter, the need for accuracy in MRI is further discussed along with an overview of some previous studies.

2.1 Magnetic resonance imaging

2.1.1 Nuclear magnetic resonance

The fundamental basis of nuclear magnetic resonance (NMR) is the behaviour of nuclear spin magnetic moments in an external magnetic field. In NMR experiments, the sample under study is placed in an external static magnetic field, B_0. This causes the magnetic moments to precess about B_0 at the characteristic Larmor frequency

$$\omega_0 = \gamma B_0, \tag{2.1}$$

where γ is the gyromagnetic ratio, specific for each nucleus. An external magnetic field causes the nuclear spin magnetic moments to align into parallel and anti-parallel states along B_0. A slight difference in the population of these states, which follows the Boltzmann distribution, causes a net macroscopic nuclear magnetization of the object. In MRI, the ^{1}H nuclei are used to produce the signal, for they are most abundant in water and fat of human tissues. The magnetization from ^{1}H nuclei in a thermal equilibrium is

$$M_0 = \frac{\rho \gamma^2 \hbar^2 B_0}{4 k_B T}, \tag{2.2}$$

where ρ is the proton number density, T is the temperature, k_B is the Boltzmann constant and $\hbar = h/2\pi$ is the Dirac constant. In equilibrium, the magnetization vector

$$\boldsymbol{M} = M_0 \hat{\boldsymbol{z}} \tag{2.3}$$

is parallel to B_0, which is by convention defined to be along the z axis.

To produce an NMR signal, a radio frequency (RF) B_1 is turned on momentarily to inject energy to the spin ensemble and tip the magnetization from equilibrium towards the transverse plane. The RF pulse frequency is determined by the Larmor frequency, as to achieve resonance. After absorbing energy from the RF pulse, the spin ensemble seeks to return to its minimum energy, thus emitting the absorbed energy to the surroundings as RF radiation. The net magnetization returns to the equilibrium value parallel to B_0. This process is called relaxation.

The relaxation of the transverse and longitudal components of the magnetization are described by the Bloch equations (see, *e.g.*, [9, 10]). If the magnetization is initially rotated to the transverse plane, the equations have solutions

$$M_\perp(t) = M_0 e^{-t/T_2} e^{i\omega_0 t} \tag{2.4}$$

$$M_z(t) = M_0 \left(1 - e^{-t/T_1}\right), \tag{2.5}$$

or in a rotating frame of reference by simply omitting the oscillating term $e^{i\omega_0 t}$ from (2.4). The constants T_1 and T_2 are the longitudal and transverse relaxation time constants. The transverse relaxation is also affected by some local field inhomogeneities, T_2', which together with T_2 form the total observed transverse relaxation, T_2^*. The transverse component of the magnetization induces an oscillating voltage in the pickup coil, which is called the free induction decay (FID) signal. The FID signal can be expressed as being proportional to

$$S(t) \propto S_0 e^{-t/T_2^*} e^{i\omega_0 t}, \tag{2.6}$$

where S_0 is the initial signal amplitude at t_0, which is proportional to the total transverse magnetization in the volume element, or voxel. [10]

In practice, the FID signal decay is quicker than the time needed to properly detect it. Thus, with a certain method, an echo signal is created and then measured and sampled. The basic types of echoes are the spin echo (SE) and gradient echo (GE) methods. An echo is created when the dephasing of spins due to the transverse decay is reversed by an RF pulse (SE method) or by switching of the gradients (GE method). The actual pulse sequences and protocols used in MRI are automated and run through by the scanner itself, but they are fundamentally based on the SE and GE techniques, or a combination of them. [10, 11, 12]

2.1.2 Spatial encoding

Spatial encoding of the NMR signal is the basis for image formation. It is achieved by making the Larmor frequencies depend on their position along an axis in the object being imaged. This is achieved with the three orthogonal gradient fields and their linear combinations that spatially and temporally vary the static field. If a gradient along the x direction is applied, the position along that axis is then frequency encoded as

$$\omega(x) = \gamma(B_0 + xG_x), \tag{2.7}$$

where

$$G_x = \frac{\partial B_z}{\partial x} \tag{2.8}$$

is the gradient in the x direction. Similarly,

$$G_y = \frac{\partial B_z}{\partial y} \tag{2.9}$$

and

$$G_z = \frac{\partial B_z}{\partial z} \tag{2.10}$$

for the y and z directions.

For a one-dimensional signal the imaging equation is

$$S(k) = \int \rho(x) e^{-i2\pi kx} dx, \tag{2.11}$$

where k is the spatial frequency due to the gradient,

$$k(t) = \frac{\gamma}{2\pi} \int G_x(t) dt. \tag{2.12}$$

The time dependence thus lies implicitly in the spatial frequencies. For a constant gradient, the spatial frequency is

$$k = \frac{\gamma}{2\pi} G_x t. \tag{2.13}$$

By applying the Fourier transform (FT) to equation (2.11), the effective spin density as a function of position is recovered, as

$$\rho(x) = \int S(k) e^{i2\pi kx} dx. \tag{2.14}$$

The above equations can be broadened to 2D and 3D imaging. Generally, the spatial frequency is then

$$\boldsymbol{k} = \frac{\gamma}{2\pi} \int \boldsymbol{G}(t) dt, \tag{2.15}$$

where $\boldsymbol{k} = (k_x, k_y, k_z)$ and equation (2.11) can be generalized as

$$S(\boldsymbol{k}) = \int \rho(\boldsymbol{r}) e^{-i2\pi \boldsymbol{k}\cdot\boldsymbol{r}} d\boldsymbol{r}. \tag{2.16}$$

The 2D or 3D signal is then likewise Fourier transformed to the spatial domain, *i.e.* the image. [10, 13]

The frequency encoding gradient is more commonly called the readout gradient, G_{RE} or G_R, and the frequency encoding direction is thus called the readout direction. In 2D and 3D images the other one or two dimensions are phase encoded respectively. The phase encoding gradients are often denoted as G_P.

Slice selection is also done using the gradients. In the beginning of each repetition, the slice select gradient is turned on in unison with the RF pulse. Thus, only the spins within the selected slice are excited. The slice thickness is affected by the applied gradient strength and the bandwidth of the RF pulse, which is the range of frequencies contained in the pulse.

2.1.3 Pulse sequences and protocols

During MRI image acquisition, pulse sequences consisting of RF and gradient pulses are applied and the signal is sampled discretely. The sampled data is collected to the acquisition matrix, or k-space, which represents the image in the frequency domain and consists of the spatial frequencies, which then via the inverse FT form the final image. The filling of k-space can be done in various ways, as the k-space trajectory is determined only by the applied gradients, as in equation (2.15). For example, cartesian, radial, or even spiral sampling methods exist, each having their own advantages and disadvantages. [13, 14, 15]

Each sequence and clinical protocol is usually designed for some specific purpose and usually some compromises have to be taken into account. For example, the BLADE technique is commonly used for motion artifact reduction (*e.g.* [14]). It uses radial k-space sampling, such that the center of k-space is oversampled. As the low spatial frequencies, *i.e.* contrast, are oversampled and then interpolated, some spatial accuracy is always lost in return. On the other hand, protocols used for *e.g.* radiotherapy planning are designed such that the imaging time is increased and some signal-to-noise ratio (SNR) is lost to maintain resolution and spatial accuracy.

2.1.4 Image resolution

The spatial resolution in MRI is defined as the size of the voxels. It thus relates to the size of the field-of-view (FOV), slice thickness, and the acquisition matrix. Similarly in 3D imaging, where the slice thickness is ”replaced” by the second phase encoded dimension. Unless the voxels are isotropic, the in-plane resolution is perceived differently depending on the viewing direction. Also, reducing the voxel size enhances the resolution, but the voxel signal strength and SNR are always reduced as a trade-off. This can be compensated, *e.g.*, by adding the number of averages, which in turn is seen as an increase in the imaging time. [10]

2.2 Geometric distortion

2.2.1 Sources of geometric distortion

To understand the geometric distortion of an MR image, it is necessary to establish an overview of the causing mechanisms. At the principle level, geometric distortion can be said to be the mismapping of spins, or a shift in the apparent location of a signal echo. This can happen due to various known reasons.

The sources that cause distortion can be divided to so called hardware related and object related sources, or sequence dependent and independent sources. The hardware related sources arise from the scanner itself and include the static field inhomogeneities and gradient nonlinearities. The object related sources arise from the patient or subject being imaged and include the magnetic susceptibility and chemical shift induced distortions.

It should be noted that, as stated in multiple studies, geometric distortion is inherently 3D in a sense that the in-plane distortion is also affected by spins outside the slice. Therefore, attention should be paid when trying to assess the true 3D distortion from 2D images. [5, 16]

Static field inhomogeneities

Most modern MRI scanners are closed bore, or cylindrical type, where the static magnetic field is created with superconducting coils. Static field inhomogeneities arise from the properties and design compromises of the coils and are one of the main reasons for distortion in the images. Spatial encoding of the signal relies on a homogenous static B_0 field, which the linear gradients then modulate creating spatial frequencies. Thus, any non-uniformity of the static field or any deviation from gradient linearity distorts the spatial frequencies, resulting in distortion in the image. [7]

The static field is purely homogenous only in theory. In reality, near-homogeneity is achieved only within a certain spherical imaging volume around the scanner isocenter. The homogeneity within this volume is usually within a few parts-per-million (ppm). [17]

The static field homogeneity is enhanced by so called passive and active shimming. Passive shimming gives a robust 'zeroth order' correction, reducing the inhomogeneity by a certain amount. It is commonly done manually, *e.g.* with metal plates fixed inside the scanner bore. As the static field strength decays with time, the passive shims need to be adjusted from time to time, which is a time consuming process. [10, 18]

Active shimming however, is more advanced, as it uses shimming coils for correcting the homogeneity. With the active shimming coils, real time corrections can be made to the field homogeneity. As every object and patient being imaged disturbs the static field, real time corrections are often required and in fact, as a part of the pre-scan routine, the scanner goes through a shimming sequence in order to make sure, that the best possible field homogeneity is achieved. The static field inhomogeneities are sequence dependent, so attention should be paid when assessing the distortion with different protocols and sequences. [10, 19]

In the figures 2.1 - 2.3, taken from Overweg (2008) [17], the relation of enhanced homogeneity to the size of the acceptable imaging volume is clearly shown.

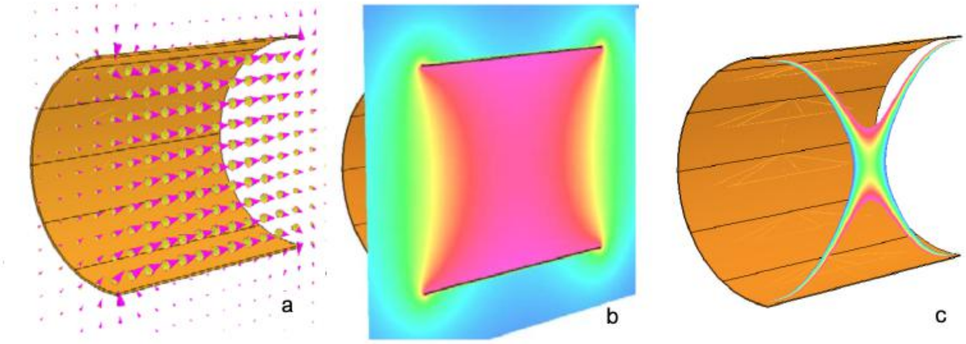

Figure 2.1: a) Field vectors of the static field in a solenoidal magnet. b) A contour map of the static field uniformity. c) Contour map of the central field with a ±1 % deviation in homogeneity, showing a volume of homogeneity not nearly large enough for imaging.[17]

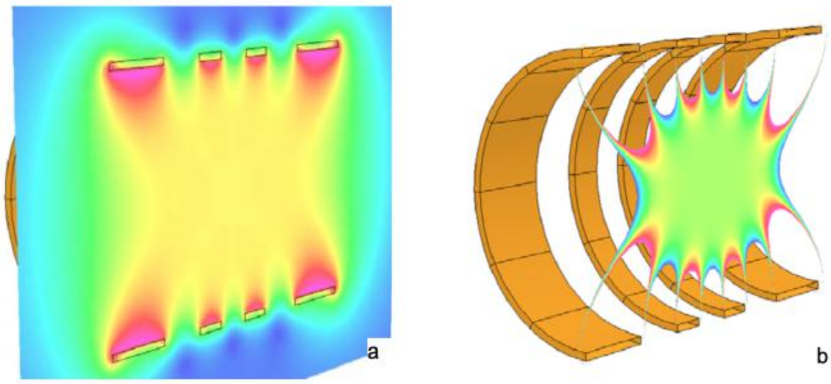

Figure 2.2: (a) A four-section magnet with the coils divided to sections showing enhanced homogeneity in the contour map. b) The central field ±1 % showing increased size of the homogeneity volume. [17]

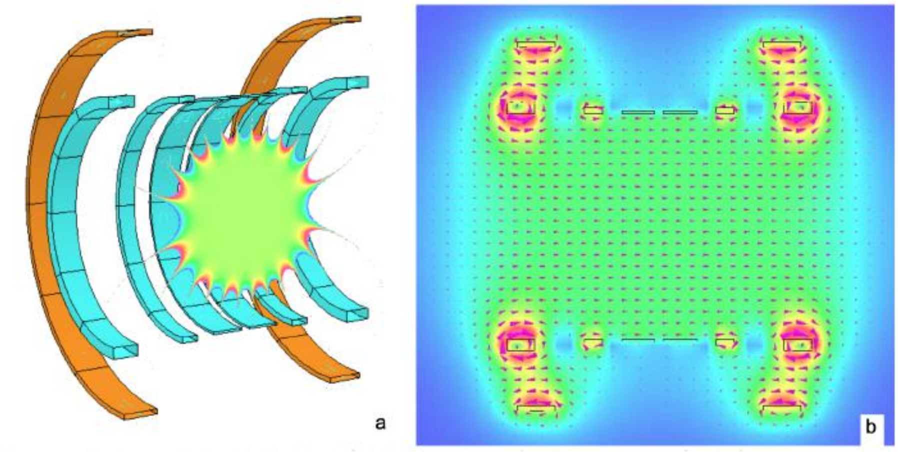

Figure 2.3: A central field contour map (a) and field vectors (b) showing further enhanced homogeneity with active shimming. [17]

Gradient nonlinearities

The gradient system consists of three orthogonal gradient fields created by the gradient coils. Although there are some different designs of coil shapes and sizes, the main purpose of producing linearly varying gradient fields for spatial encoding, is the same.

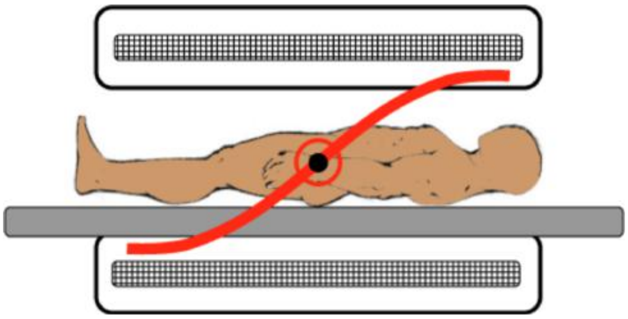

Figure 2.4: A simplified idea of gradient linearity. The linearity around the isocenter in the certain volume is acceptable, but degrades with distance from the isocenter. [20]

The gradient coils mostly produce nearly linear orthogonal modulations of the static field within a certain linearity volume around the isocenter, but as with static field homogeneity, perfection is only achieved in theory. Near perfect linearity would be achievable, but practical requirements often lead to design compromises. For example, the need for very short gradient field rise times dictate the coil design by a certain degree, at the cost of maintaining linearity. On the other hand, stronger gradients and rapid switching times induce eddy currents, which have an affect on the static field homogeneity. Also, some physiological concerns arise, such as possible peripheral nerve stimulation and loud acoustic noise. As with static field inhomogeneities, the gradient nonlinearities increase rapidly with distance from the isocenter. For a given scanner, the gradient nonlinearity distortions are sequence-independent. [19, 21, 22]

Magnetic susceptibility

In addition to the hardware related sources, there are also some object or patient related factors causing distortion in the images. Every object interacts with the magnetic field it is placed in, the magnitude of the interaction depending on its magnetic susceptibility. Magnetic susceptibility relates the magnetization of an object to the external magnetic field strength, as in

$$\boldsymbol{M} = \chi \boldsymbol{H}, \tag{2.17}$$

where χ is the volume susceptibility and $\boldsymbol{H}$ is the magnetic field strength. Susceptibility-based distortions arise notably from the boundaries of tissues or materials with different susceptibilities, such as tissue/air or tissue/bone interfaces. The magnitude of the susceptibility-induced distortion can be estimated as

$$\Delta x \simeq \Delta\chi \frac{B_0}{G_R}, \tag{2.18}$$

where $\Delta\chi$ is the susceptibility difference between two materials and G_R is the readout gradient. [19, 23, 24]

The magnetic susceptibility distortions are highly sequence dependent and the proper selection of a sequence or protocol can drastically reduce the susceptibility distortions. For example, the distortion artifacts caused by some metallic implants are often attenuated with some metal suppression sequence. [19]

Chemical shift

The chemical environment in which the nucleus is always affects the resonance frequency of the nucleus. This is called the chemical shift phenomenon. Fundamentally, it is caused by the electron magnetic moments shielding the nucleus. Instead of the external field $\boldsymbol{B_0}$, the nucleus thus experiences a total magnetic field $\boldsymbol{B}$. As a consequence, the resonance frequency of the nucleus is slightly altered, which leads to a shift in the apparent location of the echo. For different chemical environments, such as fat or water, the magnetic shielding of the nucleus varies.

The chemical shift phenomenon is very useful in pure NMR spectroscopy for determining molecular characteristics of the sample under study. It also plays a role in spectroscopic MR images, where some spectroscopic elements are included in the images. The phase shift caused by chemical shift is also used routinely in normal MR imaging to differentiate fat and water tissue. The relative difference of water and fat, in parts-per-million, remains constant at different field strengths and it can also be stated as a difference in frequency at different fields. Thus, it is directly transferable to pixels, making it a highly usable and reliable method.

Despite its advantages, the resultant distortion or apparent spatial shift remains existent in the images even when it needs not to. Like the static field inhomogeneities and magnetic susceptibility, chemical shift is also highly sequence dependent. It is manifested in the frequency encoding direction for SE and GRE sequences and may also appear in the phase encoding direction for the echo planar imaging (EPI) technique. [19, 25]

2.2.2 Distortion characterization and evaluation

Direct techniques

Geometric distortion can be defined as the spatial error or difference between the real dimensions in the object and the corresponding dimensions in the image. For example, the distance between two known and well defined points in the image should accurately correspond to the equivalent distance in the patient or a phantom. The 3D geometric distortion can be characterized by the positional errors

$$dx(x, y, z) = x'(x, y, z) - x \tag{2.19}$$

$$dy(x, y, z) = y'(x, y, z) - y \tag{2.20}$$

$$dz(x, y, z) = z'(x, y, z) - z, \tag{2.21}$$

where x', y' and z' are coordinates in the distorted space (*i.e.* the image) and x, y, and z are the real space coordinates. The distance in 3D space can then be simply expressed with Euclidean metrics

$$dr = \sqrt{dx^2 + dy^2 + dz^2}. \tag{2.22}$$

The real dimensions can be determined from the object itself, but this is of course only reliable for a phantom object consisting of, for example, a well known grid structure. [16]

Another method is to use CT images as a reference. For all practical purposes, CT images can be thought of as geometrically accurate, as the imaging technique is in a way more straight forward compared to MRI. When compared to CT, the geometric distortion can be expressed as

$$dx = dx_{MRI} - dx_{CT} \tag{2.23}$$

$$dy = dy_{MRI} - dy_{CT} \tag{2.24}$$

$$dz = dz_{MRI} - dz_{CT} \tag{2.25}$$

or simply

$$d_i = i_{MRI} - i_{CT}, \tag{2.26}$$

where $i = x, y, z$. The 3D distance can then be similarly evaluated as in (2.22).

Calculating the difference between distorted and non-distorted points is rather straight forward, but the methods used for control point identification and extraction are underscored and vary from study to another.

Indirect techniques

In addition to the direct phantom techniques, there are also some indirect techniques for evaluating and correcting the distortion. One such technique is to acquire two sets of images with the same sequence but different readout gradient polarities. The sequence-dependent distortions are sensitive to this change in gradient polarity, leading to a difference in apparent control point positions. By comparing these differences, the sequence-dependent distortions can be attained and mitigated. [19]

For example, in a 2017 study by Weavers et al. [26], the gradient non-linearity fields were studied using reversed polarity gradients. A large phantom containing small water-filled spheres was scanned with increased receiver bandwidth and two acquisitions with reversed gradient polarities, in order to mitigate the systematic off-resonance errors. By comparing the apparent shifts of the control points to a CT 'truth', the sequence-independent distortions could be attained. By iterative methods, the spherical harmonic coefficients of the gradient fields could then be estimated. The results suggested that even more accurate calibrations to the gradient non-linearity coefficients could be made, compared to the vendor corrections. [26]

2.2.3 Available correction methods

Some methods for distortion correction due to gradient nonlinearities were developed already in the 1980s [8]. Nowadays, after each sequence is acquired, the raw images are automatically filtered and corrected for some amount of distortion. For each image, a pre-determined 2D or 3D distortion correction algorithm is applied, reducing the geometrical inaccuracies. The correction methods are built in to the software and accessible to the user only such that they can be turned on or off for a particular sequence. All other software and parameters remain hidden. They utilize the direct and indirect methods discussed in the previous section, such as distortion maps calculated with the displacement errors or phase error maps created with the different readout gradient polarities. For at least the 3D correction, the scanners use some real time shimming data. Also, in some studies during the recent years, some novel distortion correction algorithms have been developed.

The correction algorithms enhance the geometrical and spatial accuracy, but not all factors can be mitigated. Some distortion is thus always present even after correction. This is called residual distortion or residual error.

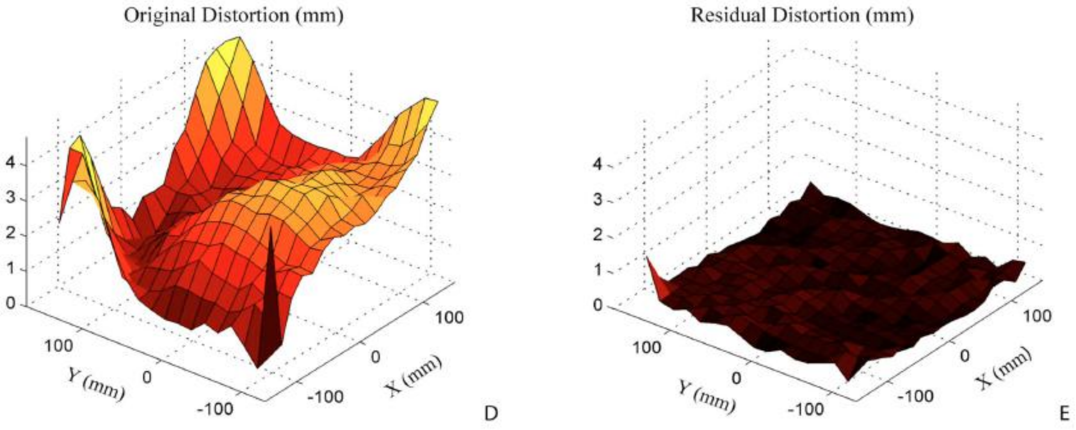

Figure 2.5: Magnitude of original distortion in an uncorrected image (left) and residual distortion after correction (right). [27]

In figure 2.5, taken from a study by Baldwin et al. [27], the magnitude of distortion in the transversal plane can be seen uncorrected (left) and corrected (right). It is clearly seen that the correction algorithm succeeds well in reducing the distortion, but not completely. Some residual error in the order of sub-millimeter remains, which is nonetheless acceptable for high accuracy demands.

2.2.4 Quality control and commercial products

The evaluation of geometric distortion is an essential part of existing MRI quality control and assurance programs. For example, the American College of Radiology (ACR) MRI accreditation program provides a multipurpose phantom for routine quality control, including testing 2D in-plane geometrical accuracy. Another commercial provider is the Computerized Imaging Reference Systems, Inc. company (CIRS), which designs, develops, and manufactures phantoms for all imaging modalities. For MRI there are, for example, the large field MRI distortion phantom, the MRI distortion phantom for stereotactic radiosurgery (SRS), and a distortion check software for automated image analysis.

2.3 Need for accuracy

Spatial and geometrical accuracy and reliability is an important aspect when using MRI for high precision means, such as radiotherapy planning or stereotactic surgery guidance. For example, geometric distortions in image-based radiotherapy planning have a direct and considerable dosimetric effect, as stated earlier. Geometric inaccuracies in excess of a few millimeters are already a concern, as unnecessary radiation dose should be avoided. [3, 19]

For neurosurgical applications, such as biopsy or electrode implantation, best achievable geometrical accuracy of the images is highly desirable, and even small inaccuracies may cause unnecessary damage during the operations. As shown by some previous studies, the in-plane geometric distortion as a function of distance from the scanner isocenter increases rapidly, reaching magnitudes of 5-10 mm even within relatively short distances from the isocenter. A magnitude of the distortion over 5 mm at a distance of 15 cm from the isocenter means that even within imaging volumes the size of the brain, notable distortions may have to be taken into consideration. Furthermore, in head imaging the center of the head is rarely located precisely at the isocenter. This can cause a pronounced difficulty for example in radiotherapy or surgery of the back of the skull. [1, 7]

For example, in a 2016 paper by Seibert et al. [28], 28 stereotactic radiosurgery cases were studied retrospectively, as it is highly dependent on accurate image guidance. A 3D correction algorithm for the gradient nonlinearities was applied to the images and the gross tumor volumes (GTV) in the corrected and uncorrected images were compared. The dose planning was done with the uncorrected images, but the actual received dose was measured with the GTVs in the corrected images. The results showed a median displacement of 1.2 mm of the GTV, minimum being 0 mm and maximum being 3.9 mm, leading to some cases fulfilling the criteria of a geometric miss. The conclusions were in accordance with previous studies, stating that although the geometric distortions in MRI are subtle and difficult to assess visually, the clinical impact of the distortions is significant.

Chapter 3

Materials and methods

In this chapter the phantom objects and the MRI scanner used are introduced. The properties and purpose, and the image acquisition process for each phantom are explained. The used image processing and analysis methods are specified.

3.1 MRI equipment and phantoms

The images for this thesis were acquired with a 3 T MRI scanner and with a total of four different phantoms, at the Oulu University Hospital. The scanner is used in routine diagnostic imaging, and for radiotherapy and high accuracy surgical planning. Some technical properties of the scanner are listed below.

Table 3.1: Some technical properties of the scanner.

Scanner	Static field (T)	Max. rms gradient strength (mT/m)	Max. rms slew rate (T/m/s)	Dimensions (cm) × (cm)
Siemens Vida	2.9	60	200	70 × 186

3.1.1 3D printed phantoms

Two prototype phantoms were previously produced with a 3D printer, with the aim of testing a novel 3D distortion grid phantom which would be suitable to be used with the head coil. The printer was an Objet30 Prime (Stratasys, Ltd.) printer. According to the manufacturer, the printing accuracy is 0.1 mm with a minimum layer thickness of 16 μm. The printing was done using a bio-compatible, MED610, material, a Windows 3D builder program, and an open-source Matlab lattice generator program for the grids. For details of the printer, materials, or the Matlab program, see [29, 30, 31].

The 3D printed 5 mm grid phantom (figure 3.1) consists of a cylinder and two grids (figure 3.2) fitted inside. The cylinder is filled with paraffin oil for signal generation. The grid thickness is 1 mm with an equal 5 mm spacing in all directions.

Another smaller 3D printed phantom prototype was a 3D printed grid inside a normal canister (figure 3.3) The grid is similar to the 5 mm grid, but considerably smaller and with a sparser 10 mm spacing. Paraffin oil was likewise used for signal generation. It should be noted, that this prototype was really a rather rudimentary piece for testing the effect of the increased grid spacing from 5 mm to 10 mm.

Figure 3.1: The 3D printed cylinder.

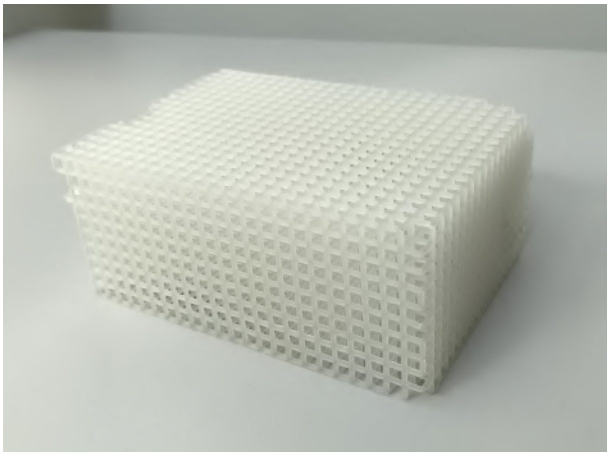

Figure 3.2: A sample piece of the 3D printed 5 mm grid.

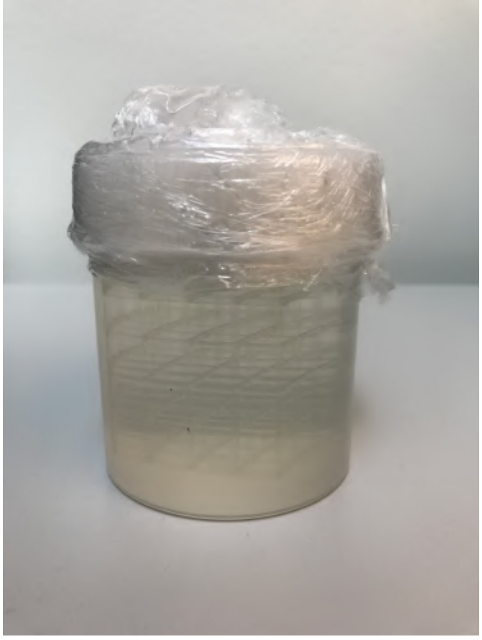

Figure 3.3: The prototype 10 mm grid inside a canister.

3.1.2 Commercial phantoms

In addition to the two 3D printed prototype phantoms, two commercial phantoms, the CIRS large field distortion phantom and the ACR phantom, were used.

The CIRS large field MRI distortion phantom (from now on, the CIRS phantom) is designed for routine assessment of 3D distortion caused by the nonlinear magnetic field. The phantom (figure 3.4) consists of a plexiglass cylinder, which contains an orthogonal 3D grid inside the volume. The cylinder is 300 mm in length, 276 mm in height, and 330 mm in diameter. The grid consists of plastic rods 3 mm in diameter, spaced 20 mm apart. The cylinder can be filled with a signal-generating solution, such as water or paraffin oil, although when filled with water, imaging in a 3 T field produces strong dielectric artifacts (*e.g.* [32]). It can be also be emptied for CT imaging, in which the grid/air interface provides good contrast. For purposes of this thesis, the cylinder was filled with paraffin oil, essentially to avoid dielectric artifacts.

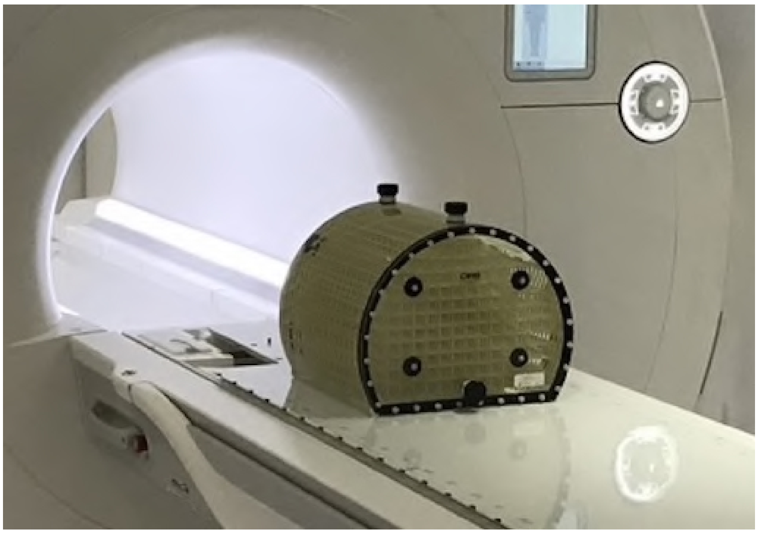

Figure 3.4: The CIRS large field distortion phantom.

Another commercial phantom, the ACR phantom (figure 3.5), is a closed acrylic plastic cylinder, with an inside length of 148 mm and inside diameter of 190 mm. The cylinder is filled with a mixture of $NiCl_2$ and NaCl for signal generation. Inside the cylinder are multiple structures for a variety of scanner performance tests, such as central frequency, transmitter gain or attenuation, and spatial resolution. For testing the geometric accuracy there is a sparse grid, which by itself is only meant to be visually inspected from the images, but it can also be used as means of locating a few control points. As the phantom is a multipurpose one, the grid meant for geometric accuracy assessment is only a 2D grid. This is a limitation, because of the 3D nature of the distortion, and it will be discussed later. Also, if images from multiple orientations need to be acquired and compared, the phantom needs to be repositioned on the table, which means degraded reliability and comparability. [33]

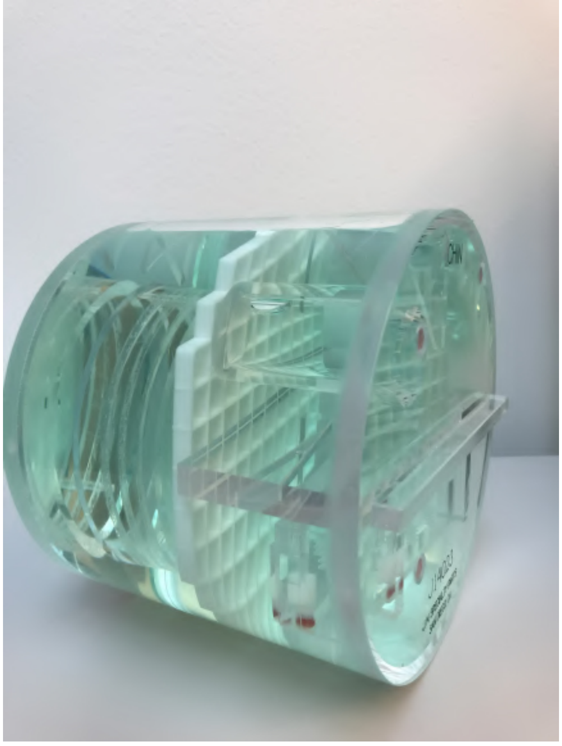

Figure 3.5: The ACR MRI phantom. The distortion grid is visible in the middle.

3.2 Image acquisition

3.2.1 3D printed phantoms

Images of the 3D printed grid phantoms were acquired using a 64-channel head coil and two different 3D sequences. The two sequences, MPRAGE and SPACE, were chosen on the basis that they are commonly used 3D volume sequences for high resolution isotropic head imaging. The MPRAGE sequence is essentially a T_1-weighted 3D rapid gradient echo sequence added with an inversion recovery (IR) pulse for better contrast, whereas the SPACE sequence is a T_2-weighted 3D fast spin echo sequence with very short echo times and long echo train lengths.

3D printed 5 mm grid phantom

With this phantom, images from all three principle directions were acquired with both sequences. One of the original aims was to test the effect of slice orientation and sequence to the amount of distortion. In addition, one transversal slab with MPRAGE was acquired with the body coil for possible comparison of the receiving coil.

For both sequences an acquisition matrix of 512 x 512, FOV 256 mm x 256 mm, and slice thickness of 0.50 mm were chosen, giving an isotropic voxel size of $0.50 \times 0.50 \times 0.50$ mm^3. The grid thickness is 1.0 mm, so the isotropic voxel size needed to be small enough for the resolution to suffice for feature extraction. A better resolution would have been beneficial, but technical matters in the sequence design limited the acquisition matrix size giving the in-plane resolution of 0.50 mm. Also, the SNR becomes a concern with decreasing voxel sizes and the number of averages would have to be increased to maintain the SNR, leading to unreasonably long imaging times.

The slices from all directions were then reformatted to the transversal orientation for comparability and also to align the slices more accurately with the grid structure of the phantom.

3D printed 10 mm grid phantom

Similar to the 5 mm grid, the 10 mm grid was also imaged with a 64-channel head coil and with the MPRAGE and SPACE sequences. Unlike the 5 mm grid, only the transversal slabs were acquired, with two different resolutions for both sequences. The same FOV of 256 mm x 256 mm was chosen, with two different acquisition matrix sizes of 256 x 256 and 512 x 512, with a slice thickness of 1.0 mm and 0.5 mm respectively. Thus, the voxel sizes were once again isotropic 1.0 x 1.0 x 1.0 mm^3 and 0.5 x 0.5 x 0.5 mm^3.

3.2.2 Commercial phantoms

ACR phantom

For the ACR phantom, a large FOV geometric distortion quality assurance method by Siemens was used [34]. The phantom was placed upwards on the scanner table, such that the grid structure (fig. 3.5) was oriented in the coronal direction. Then, the grid was imaged with the body coil and a high resolution 2D spin echo sequence with 550 x 550 mm FOV, 512 x 512 acquisition matrix and slice thickness of 5 mm. The scanner table was programmed for automatic movement between sequences such that five coronal images with the same FOV but different grid position were acquired. This was repeated with different phantom positions along the x-direction. The images were then added together using an arithmetic mean function, a property of the scanner software. This way, the resulting image consisted of the grid structure filling a large FOV and visible distortion at the edges (see results).

CIRS large field phantom

The images of the CIRS large field phantom were acquired in collaboration with the department of radiation therapy, for their own quality control purposes. The phantom was placed on the scanner table as in fig. 3.4, using the body and spine coils as receiving coils. The selected images used in this thesis are coronal slices acquired with a 2D turbo spin echo sequence. The slice thickness was 0.9766 mm and a FOV of 500 mm x 500 mm and a 512 x 512 acquisition matrix gave the resolution of 1.0240 pixels per mm.

3.3 Image analysis

For image analysis, two different tools were used. One, meant to be used with all phantoms, was an in-house Matlab program. The program was made previously for upcoming studies and testing of the 3D printed prototype phantoms. The core purpose of the script is to take an image of a grid, extract the rod intersection points, compare them with a non-distorted ”true” lattice, and return the difference of the points in pixels as well as the direction of the point shifts. Starting from the middle of the image, the central horizontal and vertical rods are found using the corresponding horizontal and vertical grayscale profiles, in which the local minima represent the smallest grayscale values, *i.e.* the rods. Beginning from the center, each rod found are traced separately in each direction, combining them into lateral and vertical sequences of points. These sequences are then smoothed with polynomial interpolation, such that the effect of the ratio of resolution to rod thickness would be less emphasized. From these smoothed point sequences, the grid intersection coordinates are then extracted. Finally, the intersection point closest to the center of the image is chosen, and an ideal non-distorted point lattice is generated according to a known preset grid distance. The difference in pixels between the corresponding non-distorted and distorted points are then calculated, as in section 2.2.2.

Another analysis software used was the CIRS distortion check program, an online cloud-based application meant to be used for the CIRS phantoms. It features fully automated detection of all grid intersections and control points for comparison with a CT ’truth’. After interpolation, 3D distortion vector fields are generated. The resulting distortion fields can be reported for example as scatter plots or contour plots. [35]

Additionally, an open-source image processing program ImageJ was used for image viewing and plotting some rudimentary line intensity profiles, which will be seen in the next chapter.

Chapter 4

Results and discussion

In this chapter the relevant images and subsequent analysis are presented, along with simultaneous discussion and notices. Some main limitations are emphasized, along with some comparison of the different methods and results. Finally, possible improvements and future studies are briefly discussed.

4.1 3D printed 5 mm grid phantom

The 5 mm grid prototype phantom was imaged with different sequences, coils and orientations with a variety of things in mind. In figures 4.1a and 4.1b, two slices of the transversal MPRAGE slab are shown. The images are precise and the good amount of averages gives great SNR and contrast despite the small voxel size. Rather surprisingly however, the Matlab script was unable to produce sensible results. There were always, for example, some point sequences not finding the local minima and the middle of the rod, which was a fundamental difficulty. The reason traces to the ratio of resolution to the grid dimensions, especially the rod distances. To illustrate, in figures 4.2 - 4.4, the grey value intensity profiles are plotted from two different positions. In figure 4.3, the effect of the grid being too dense is shown. The local minima and maxima are too close to each other and as derivatives of the profile are also used, problems arise. On the other hand, as seen in figure 4.4, the local minima are almost indistinguishable from the base line.

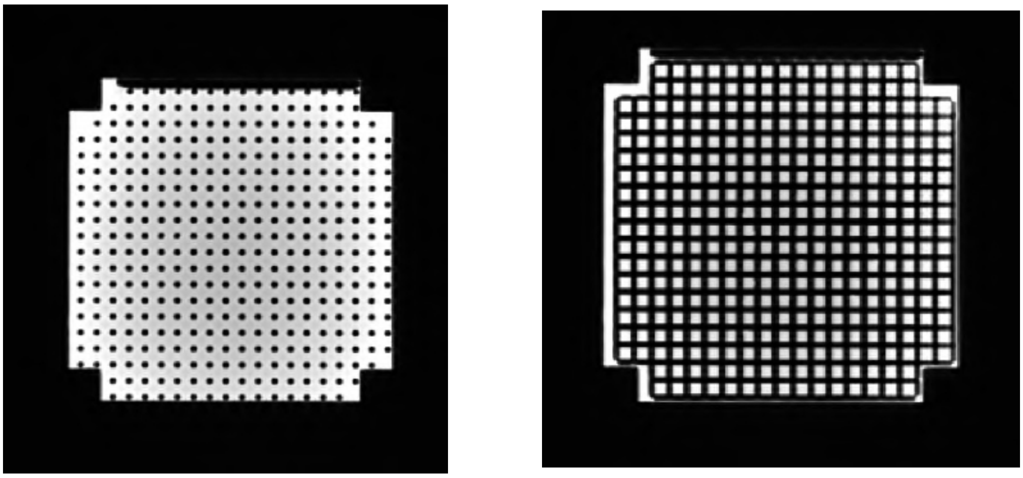

(a) (b)

Figure 4.1: Transversal MPRAGE images of the 5 mm grid phantom with one slice from between the rods (a) and one including the in-plane rods (b).

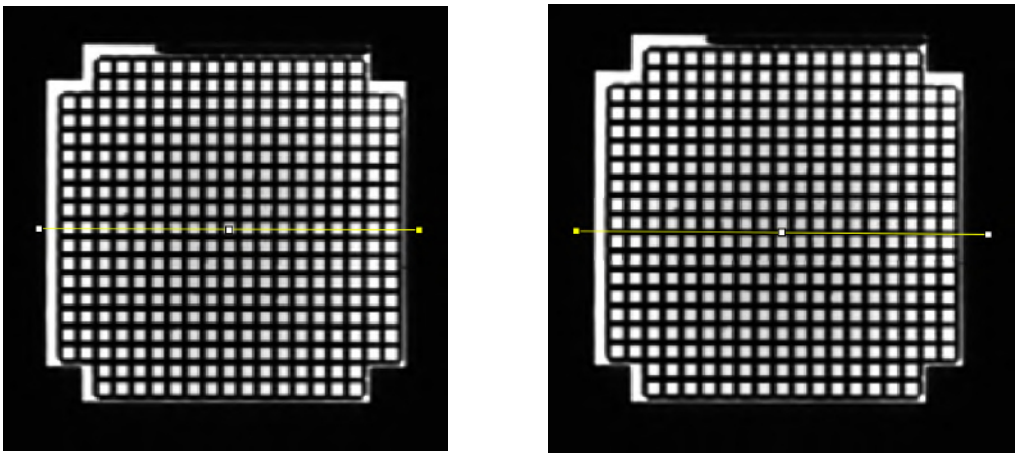

(a) (b)

Figure 4.2: Positions which the intensity profiles in figures 4.3 and 4.4 are plotted along, shown by the yellow lines.

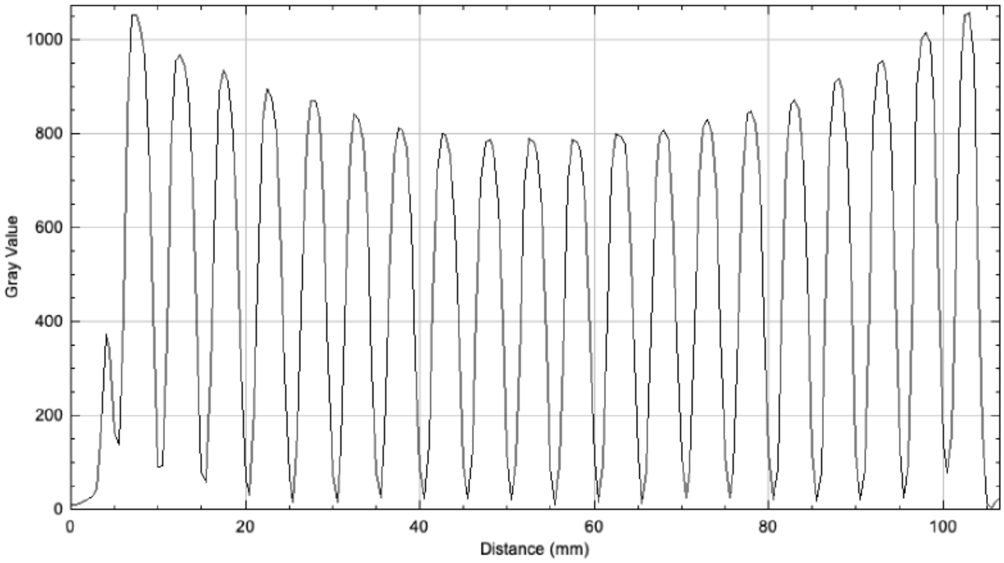

Figure 4.3: Grey value intensity profile for fig. 4.2a.

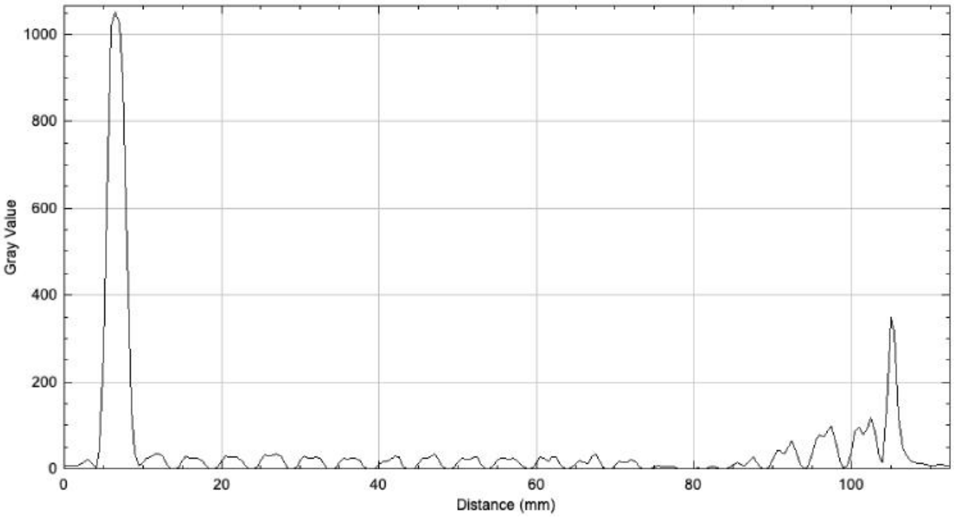

Figure 4.4: Grey value intensity profile for fig. 4.2b.

4.2 3D printed 10 mm grid phantom

The images of the 10 mm grid phantom were not taken through the Matlab program, but preliminary results were more promising, as for the grid density and the intensity profiles. In figures 4.5a and 4.5b, the higher resolution images of both sequences are shown. As is clearly seen, widening the grid spacing from 5 mm to 10 mm makes a remarkable difference. The intensity profiles are again plotted for both along the yellow lines shown. The profiles for 4.5a and 4.5b are shown in figures 4.6 and 4.7 respectively. Now, the local minima are clearly distinguishable. The rods are thin enough and far apart to be distinguishable even with lower resolution. Unlike with the 5 mm grid, the ratio of grid density to resolution is not so much of a concern here. It should be noted, that the apparent grid warping in both images is not due to geometric distortion, but simply because of the interaction of the grid material with the filling oil. This is, again, one more problem of a kind and will be discussed further.

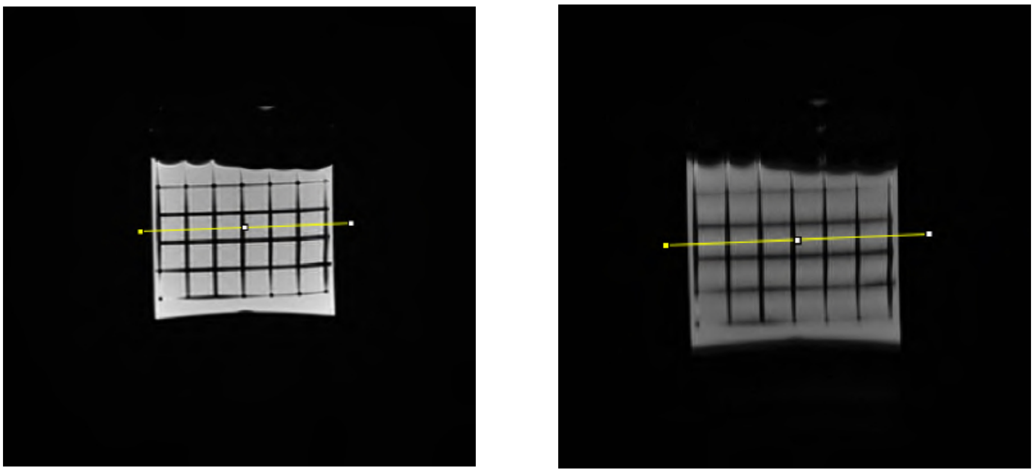

(a) (b)

Figure 4.5: Transversal MPRAGE (a) and SPACE (b) images of the 10 mm grid phantom.

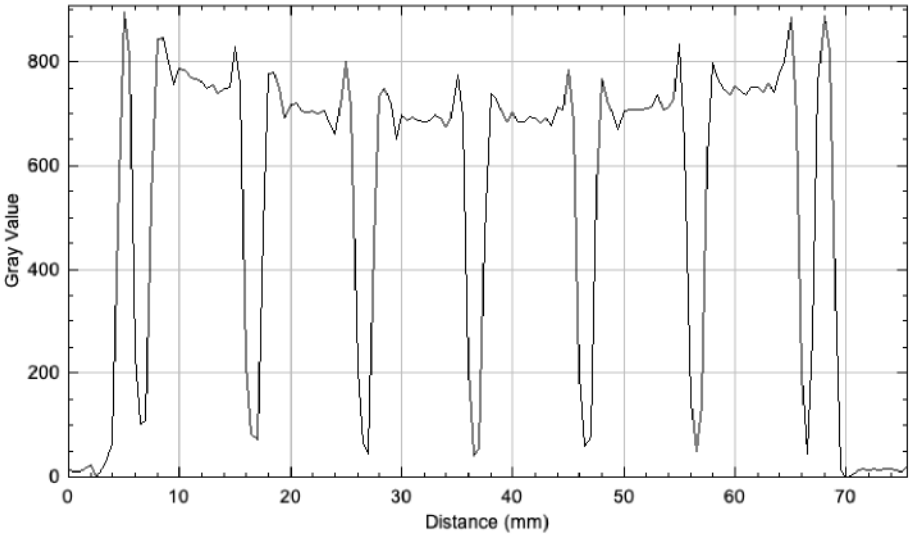

Figure 4.6: Intensity profile of the MPRAGE image, plotted along the yellow line in figure 4.5 (a).

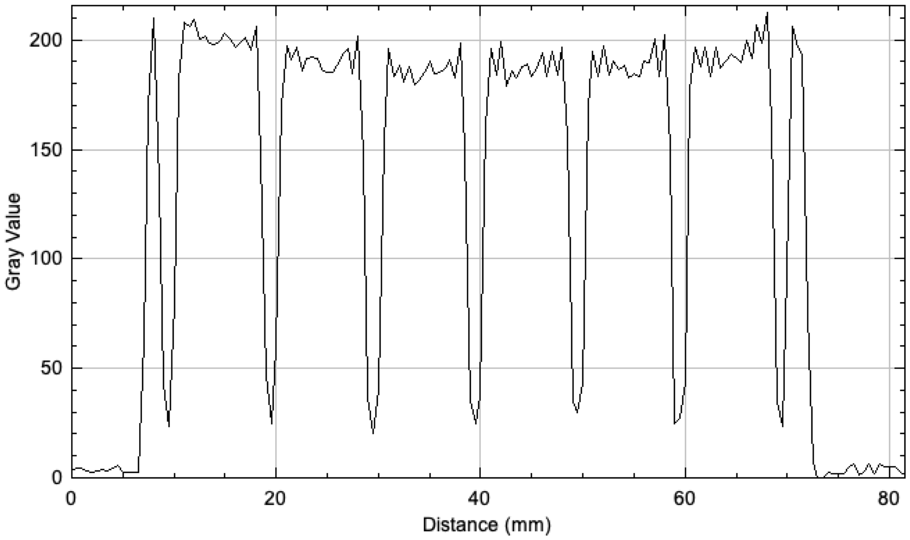

Figure 4.7: Intensity profile of the SPACE image, plotted along the yellow line in figure 4.5 (b).

4.3 The ACR phantom

Images of the ACR phantom were analyzed with the Matlab script and the results can be seen in figures 4.8 - 4.11. In figure 4.8, the vertical and horizontal point sequence and polynomial interpolation curves are shown. As can be seen, the areas around the center of the image are rather immaculate, but at the edges and more faded areas, problems occur.

In figure 4.9, the displacement vectors for almost each control point are shown. The residual geometric distortion manifests itself clearly at the top and the bottom as the warping of the grids. The most outward left and right columns of points should be neglected, as they are miscalculated (shown also in figure 4.8). At the center of the image the distortion is practically non-visible and growing in magnitude towards the edges, as it of course should be, based on our existing knowledge. Due to the large FOV in figure 4.9, the displacement vectors are only clearly distinguishable when 'zoomed in', as in figure 4.10. The distortion shifts are in the order of one to two pixels, which, estimated from the resolution, account to an order of one to two millimeters in magnitude of the residual distortion.

Finally, the magnitude of the distortion for each point is shown in figure 4.11a and the relative direction of the shift in radians in figure 4.11b, with the respective color codings. Although the grid covers a relatively large FOV in the coronal plane, the magnitude of the distortion remains rather moderate. Only at the edges, visible distortion and warping of the grids can be seen. On the other hand, those areas are not covered by the algorithm. Additionally, it should be once again emphasized, that only the 2D in-plane distortion can be evaluated. This means, in essence, that even though a pixel could be shifted in the sagittal plane, only a projection to the coronal plane of the total shift is seen. If a better understanding is wanted, the phantom needs to be imaged from all directions and at different heights in order to form even a decent picture of the 3D distortion field.

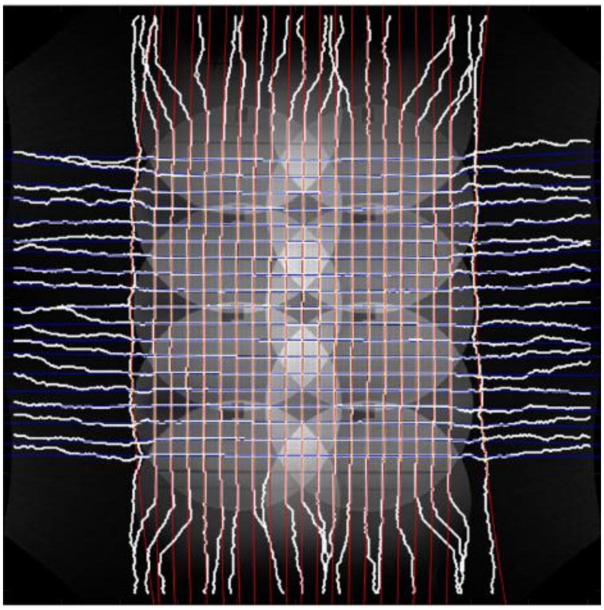

Figure 4.8: The horizontal and vertical line finding point sequences and polynomial interpolation curves.

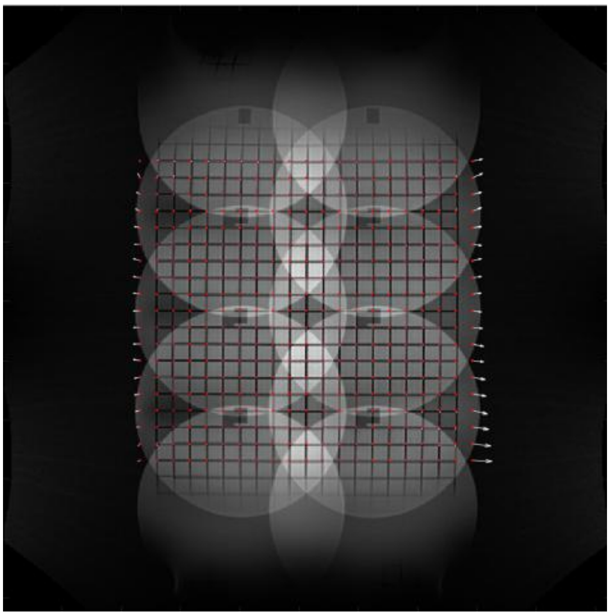

Figure 4.9: The displacement vectors for each recognized intersection point.

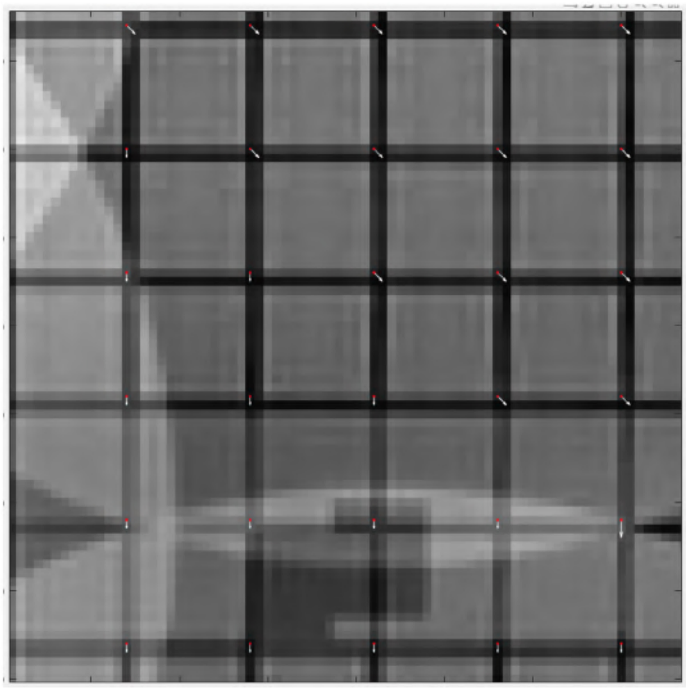

Figure 4.10: A zoomed in capture from figure 4.9 elaborating on the displacement vectors.

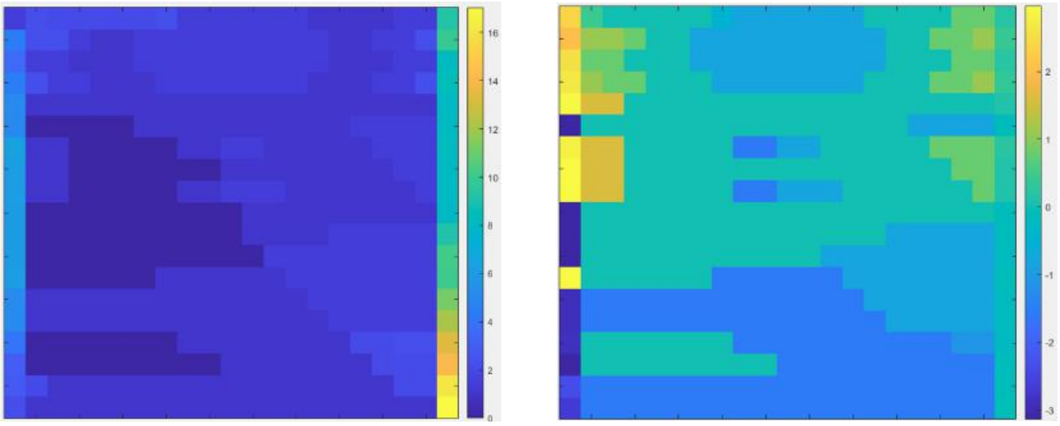

(a)

(b)

Figure 4.11: The magnitude in pixels (a) and direction in radians (b) of each displacement in figure 4.9.

4.4 The CIRS phantom

The CIRS phantom images were analyzed with two different tools, the Matlab program and the CIRS distortion check software. Thus, some comparability and cross check could be done. As to the Matlab program, in the coronal image in figure 4.12, the line finding curves are seen, along with the distortion manifested as warping at the edges. Except for the bottom row and the rightmost column, the grid is recognized properly. In figure 4.13, the displacement vector field is seen. Now, even with a large FOV image, the distortion shifts can be clearly seen. The distortion is negligible at the center of the image, but once again growing in magnitude towards the edges, as expected. Likewise, in figure 4.14a, the magnitude of distortion in pixels is shown, along with the direction of the shift in radians in figure 4.14b. In both 4.13 and 4.14b, the change of direction in the shift is shown.

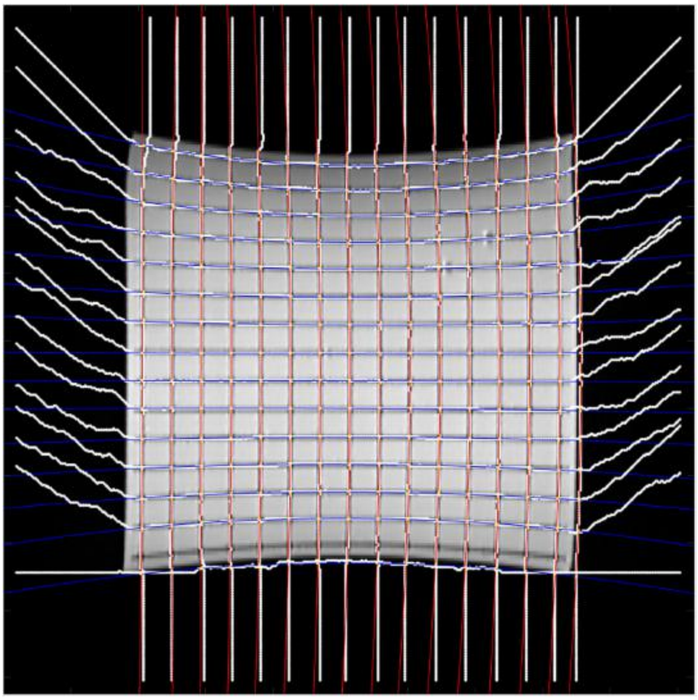

Figure 4.12: The line finding curves for the CIRS phantom.

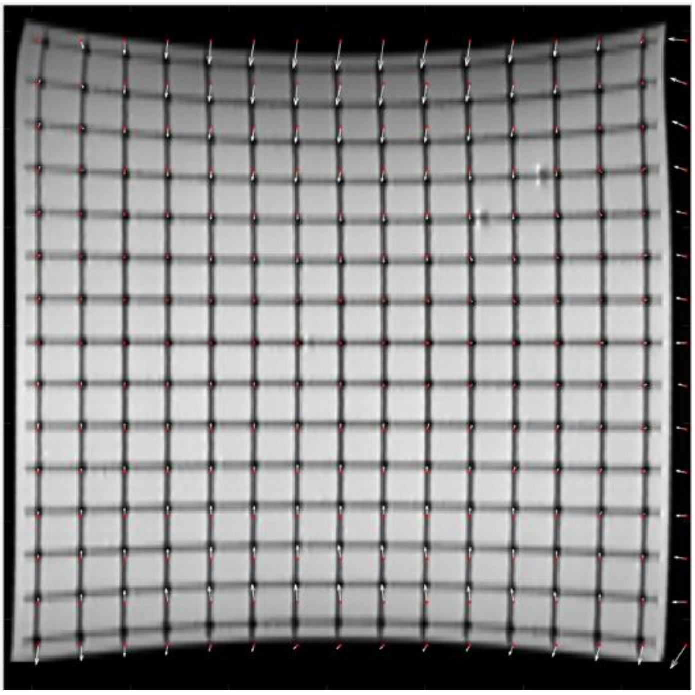

Figure 4.13: The displacement vector field.

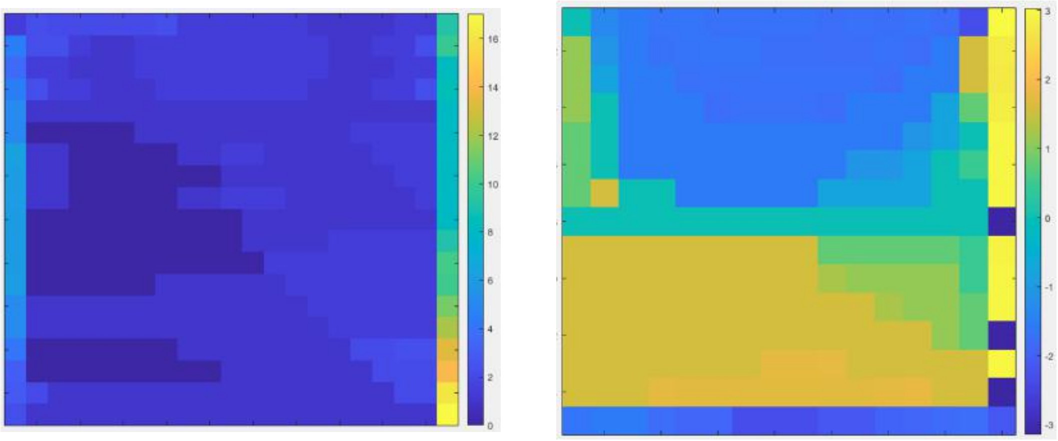

(a)

(b)

Figure 4.14: The displacement magnitudes in pixels (a) and direction in radians (b) for each control point.

The CIRS distortion check software provided a full analysis report containing basic data acquisition information, contour plots for all three principal orientations, scatter plots, and error tables. From these, a few selected figures are shown here. In figure 4.15, a coronal contour plot of the distortion magnitude is shown. The sudden increase in the distortion magnitude at large z values, *i.e.* the top of the plot, is due to shielding plates of the scanner room wall, close to the opening of the scanner bore. A comparison between figures 4.14a and 4.15 is not facile, but some similarities at least in the order of magnitude can be pointed out, such as the distortion growing in magnitude from the center towards the edges and the amount of distortion being in the order of 1 to 2 pixels or 1 to 3 millimeters.

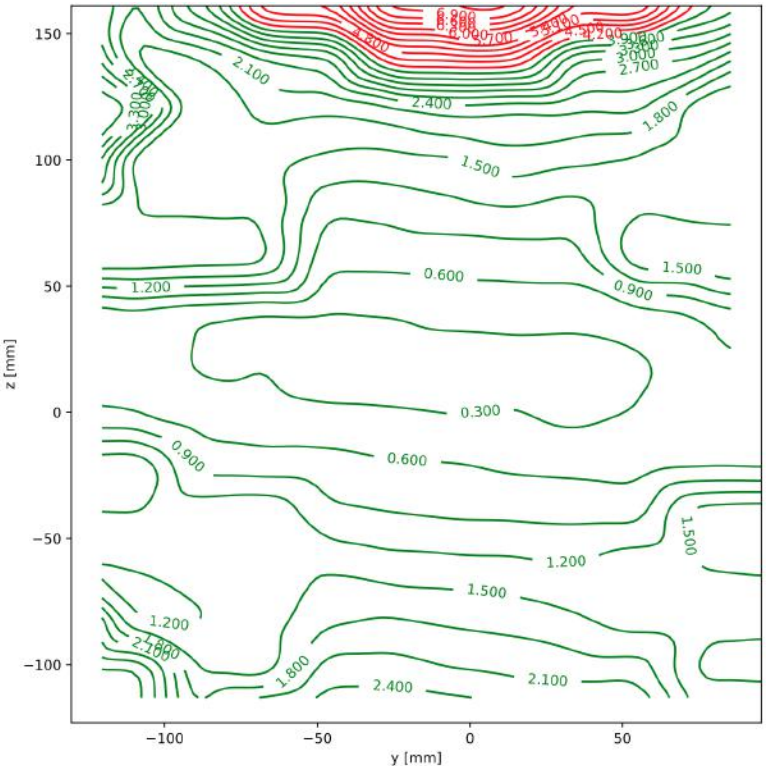

Figure 4.15: Coronal contour plot.

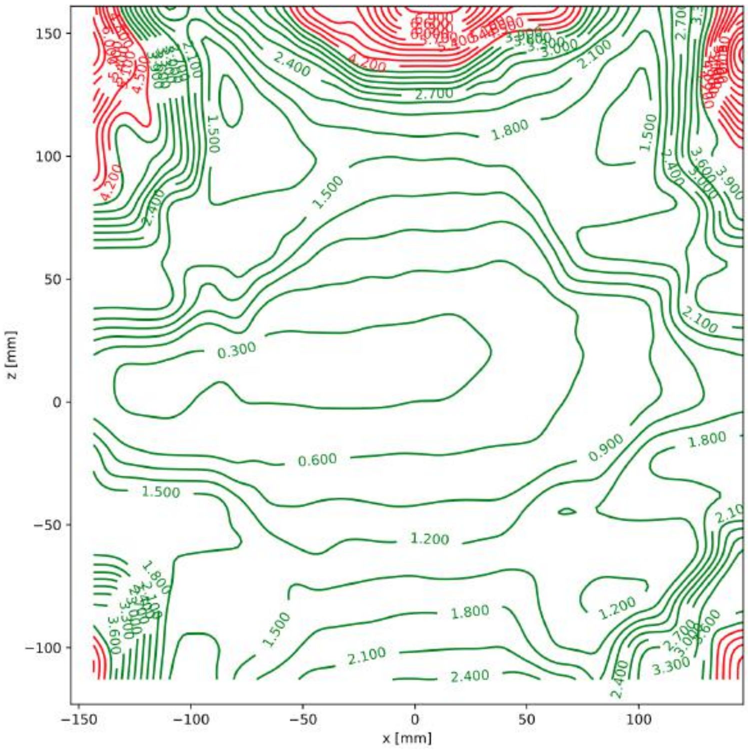

Figure 4.16: Sagittal contour plot.

In figure 4.16, the sagittal contour plot is shown. The shape of the distortion field and the resemblance with the static field homogeneity contour plot in figure 2.3 is notable. The effect of the scanner room shielding plates can be seen, similar to figure 4.15. In figure 4.17, a scatter plot of the distorted control points as a function of the distance from isocenter is shown. The plot complies with the fact that the distortion grows in magnitude with distance from the isocenter. This was predicted and in accordance with previous studies. A question about the reason for the apparent clustering of the points, especially at greater distances from the isocenter, should be asked. It is possible that the clustering is purely coincidental, so caution should be used not to draw false conclusions from it. Nevertheless, it should be noted that the scatter plot contains the distortion magnitudes from the whole phantom volume projected to a 2D plot. Thus, information about the relative positions are lost and any conclusions about two adjacent points on the scatter

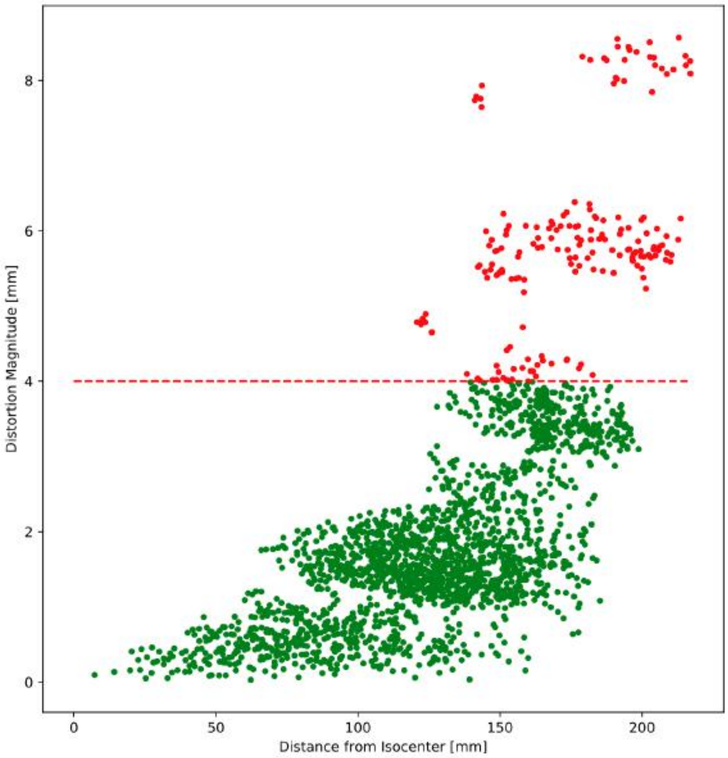

Figure 4.17: Scatter plot of the distortion as a function of distance from the isocenter.

plot being close to each other in real space should not be made. Still, a reasonable idea of the distortion magnitude as a function of distance from the isocenter can be obtained. Also, some comparison between the Matlab-based distortion field in figure 4.13 with the coronal contour plot in figure 4.15, can be made. Visually the two are, at least approximatively, in accordance with each other. Likewise, the distortion magnitudes from the Matlab distortion field, the contour plots, and the scatter plot are all in the same order of a few millimeters, as expected. The red line at 4 mm of distortion magnitude in the scatter plot can be taken as some kind of acceptable limit. Clearly, most control points remain under that amount of shift.

4.5 Summary of main results

The results for each phantom were already briefly discussed in their respective sections, but a summary is still beneficial. As to the 3D printed phantoms, the effect of grid density was realized. It was concretized with the 5 mm grid, in that even with the best achievable resolution, the intensity profiles were too dense for the Matlab algorithm to perform reasonably. The inadequacy of a grid too dense was not stated in any previous study undergone for this thesis, at least not explicitly. It could probably have been foreseen in theory by comparing the needed resolution to the grid density, but in this case only the preliminary results revealed the reality of the situation. The 10 mm grid was then tested with more promising signs. The grid density was better, as estimated from the intensity profile, and it would probably be sufficient even with a lower resolution. The purpose itself of evaluating the geometric distortion with the Matlab script was not achieved with either prototype phantom.

The ACR phantom provided little value to the entity, mostly serving as a means for methodological comparison and as some kind of a test for the Matlab script. The coronal large FOV image was analyzed with the Matlab script, which provided some information of the coronal in-plane distortion field, being in the order of a few millimeters in magnitude throughout the plane.

The CIRS phantom was analyzed with both the Matlab script and the distortion check software. These both provided sensible and good results and a quantitative evaluation of the residual geometric distortion was obtained. The results were as expected, the magnitude of the distortion being mostly under the somewhat acceptable 4 millimeters within a radius of 150 millimeters around the isocenter. Also, the geometrical behaviour of the distortion field was rather as expected.

4.6 Limitations and method comparison

During the image acquisition and analysis phase, the issues and limitations of each phantom and method became clear and were further underlined by the results. In addition to the problem of grid density in the 3D printed grid phantoms already discussed, some other issues also appeared. The 5 mm grid phantom turned out to be difficult to orientate during imaging, which also directly relates to the difficulty of reasonable slice orientating. Likewise, acquiring slices perfectly along the grid structure turned out to be rather difficult. This was bypassed by reformatting the 3D images to align with the grid structure but still, the ambiguousness of positioning the phantom and reformatting the images are not desirable, as they worsen the repeatability and reliability of consequent tests. Another fundamental limitation, as with all 3D printing, is the fact that the printer size and properties lay obvious constraints to the object size and dimensions, as well as for the materials used in it. The printing material and the signal-generating solution need to be carefully chosen. As briefly mentioned already, the 10 mm grid was slightly deformed due to the oil penetrating the grid material. The grid had been inside the oil-filled canister for around 2 years already, resulting in the now visible deformation in the images, as opposed to the 5 mm grid being much newer and in immaculate condition. This then of course poses a serious limitation to the usability of all possible 3D printed grid phantoms, as the method of determining the distortion shifts from the control points in the distorted space relies on the fact that the grid is in fact rigid and orthogonal in real space.

As to the Matlab script, issues with the line finding algorithm were encountered and seen all the way in the final results. Another issue worth pointing out is the fact, that in generating the non-distorted reference lattice, the script chooses an intersection closest to the center of the FOV. This means, in essence, that an implicit assumption of the isocenter coinciding with the center of the image is made. This of course is generally not the case, even with careful positioning of the phantom. The uncertainty and error caused by this means that it is probably wiser to look at the distortion map as a whole, instead of examining each control point and their respective distortion shifts individually.

For the ACR phantom, the fundamental limitation of the 2D grid structure was discussed earlier. It should still be emphasized, that the phantom is strictly speaking not meant to be used for 3D distortion evaluation, but only for some coarse and visual slice geometry checks, as also mentioned earlier. This means that calling the 2D grid structure a limitation is purely a matter of choice and dependent on the purpose of its use. Still, in the context and aim of this thesis, the grid structure can be considered as a limitation. Comparison of the ACR phantom with the CIRS phantom, another of the two commercial ones, should be made carefully. As the ACR phantom is in essence a multipurpose one and the CIRS phantom is purposefully made for 3D distortion evaluation, a strict comparison of these two would be unfair. To mention one issue with the CIRS phantom, would be the emergence of dielectric artifacts in a 3 T field, when the phantom is filled with water. This was bypassed by filling the phantom with paraffin oil, which turned out to be an inconvenience of a kind and strictly speaking a procedure not completely 'by the book'. Nevertheless, as to the purpose of distortion evaluation, the CIRS phantom was superior in every other sense.

Finally an issue worth pointing out in a more general sense, common to all the phantoms used, is that no real evaluation of patient-induced distortions can be made. This should not be neglected, as a temptation to apply direct corrections to patient images from phantom images could appear. The sources of geometric distortions are, at least ideally, separable from each other. In a real image however, the distortion shifts are a sum of all the contributions of the causing mechanisms of distortion. Unless explicitly taken into account during image acquisition, *e.g.* with the reverse gradients method, evaluating individual contributions of different distortions from the image is not reasonable by any means.

4.7 Possible improvements and future studies

Based on the results and some limitations already discussed, improvements and aims for possible future studies can be underlined. As discussed in the previous section, one sort of limitation with the 3D printed phantoms was the lack of positioning aids, which would have facilitated orienting the grid along the principal axes and coinciding the grid center with the scanner isocenter. In essence, all future phantoms should be designed with easy positioning and orientating in mind. On the other hand, this means that a phantom placeable both inside a head coil as well as on the scanner table is hard to design. For real quality control purposes, repeatability and reliability are key in validating the phantom for routine use.

For future studies, the evident next step would be to test the 10 mm grid structure but in larger scale. A simple design, similar to the 5 mm grid phantom, would be for example a printed 10 mm grid placed inside a cylinder or a box. Thus, the Matlab script could also be further tested. As to the Matlab script itself, the next step would be trying to include the third dimension to the reference lattice and the distortion shifts. For the water-filled CIRS phantom, the cause of dielectric artifacts at 3 T field could be looked into. Also, other commercial products, such as the CIRS MR distortion and image fusion head phantom, could be tested and used.

In any case, as soon as a a phantom and an analysis software is chosen, be it a validated in-house phantom and the Matlab script or a commercial solution, there would then be several aspects of interest to look into. The ideas suppressed in the context of this thesis, such as the effect of slice orientation, imaging sequence, or field strength, could then be studied.

Chapter 5

Conclusions

In this thesis different phantoms and analysing tools were tested and the residual geometric distortion of one selected 3 T MRI scanner was assessed quantitatively with a commercial distortion check software and a Matlab script. The 3D distortion shifts within a radius of 100 mm from the isocenter were mostly 2 mm or less. Shifts below 4 mm were encountered up to 200 mm, with occasional shifts up to 9 mm between 100 and 200 mm from the isocenter. Distortion field maps and contour plots produced with both analysis methods seemed to be in accordance with each other. The distorted field geometry and behaviour was as expected on the basis of theory and previous studies. Additionally, with regard to prototype phantom testing, a problem with grid density was discovered. A 5 mm grid spacing was not sparse enough with the achievable imaging resolution and the used analysis method. The tested 10 mm grid spacing indicated more promising preliminary results and provided insight for future testing. Based on the experiences with different phantoms and softwares, it is suggested that the available commercial solutions should be considered instead of iterating and testing alternative prototype solutions. Although seemingly well-defined and straightforward at first, the questions surrounding the subject and field require careful thought to every aspect. In this regard, valuable experience for future studies was gathered. Whether the perfect phantom and analysis software is developed, or a well-defined standard for distortion check in MRI quality control will be made, remains to be seen.

Bibliography

[1] D. B. S. for Parkinson's Disease Study Group, "Deep-brain stimulation of the subthalamic nucleus or the pars interna of the globus pallidus in parkinson's disease," *New England Journal of Medicine*, vol. 345, no. 13, pp. 956–963, 2001.

[2] C. Menuel, L. Garnero, E. Bardinet, F. Poupon, D. Phalippou, and D. Dormont, "Characterization and correction of distortions in stereotactic magnetic resonance imaging for bilateral subthalamic stimulation in parkinson disease," *Journal of neurosurgery*, vol. 103, no. 2, pp. 256–266, 2005.

[3] E. P. Pappas, M. Alshanqity, A. Moutsatsos, H. Lababidi, K. Alsafi, K. Georgiou, P. Karaiskos, and E. Georgiou, "Mri-related geometric distortions in stereotactic radiotherapy treatment planning: evaluation and dosimetric impact," *Technology in cancer research & treatment*, vol. 16, no. 6, pp. 1120–1129, 2017.

[4] J. Slagowski, Y. Ding, Z. Wen, C. Fuller, C. Chung, M. Kadbi, G. Ibbott, and J. Wang, "Quantification of geometric distortion in magnetic resonance imaging for radiation therapy treatment planning," *International Journal of Radiation Oncology, Biology, Physics*, vol. 102, no. 3, p. e547, 2018.

[5] T. Torfeh, R. Hammoud, G. Perkins, M. McGarry, S. Aouadi, A. Celik, K.-P. Hwang, J. Stancanello, P. Petric, and N. Al-Hammadi, "Characterization of 3d geometric distortion of magnetic resonance imaging scanners commissioned for radiation therapy planning," *Magnetic resonance imaging*, vol. 34, no. 5, pp. 645–653, 2016.

[6] M. Jafar, Y. M. Jafar, C. Dean, and M. E. Miquel, "Assessment of geometric distortion in six clinical scanners using a 3d-printed grid phantom," *Journal of Imaging*, vol. 3, no. 3, p. 28, 2017.

[7] D. Wang and D. M. Doddrell, "Geometric distortion in structural magnetic resonance imaging," *Current Medical Imaging*, vol. 1, no. 1, pp. 49–60, 2005.

[8] G. H. Glover and N. J. Pelc, "Method for correcting image distortion due to gradient nonuniformity," May 27 1986. US Patent 4,591,789.

[9] F. Bloch, "Nuclear induction," *Physical review*, vol. 70, no. 7-8, p. 460, 1946.

[10] D. W. McRobbie, E. A. Moore, M. J. Graves, and M. R. Prince, *MRI from Picture to Proton*. Cambridge University Press, 2nd ed., 2007.

[11] E. L. Hahn, "Spin echoes," *Physical review*, vol. 80, no. 4, p. 580, 1950.

[12] A. D. Elster, "Gradient-echo mr imaging: techniques and acronyms.," *Radiology*, vol. 186, no. 1, pp. 1–8, 1993.

[13] S. Sỳkora, "Kspace formulation of mri," *Stan's Library, Ed. S. Sykora*, vol. 1, pp. 11–21, 2005.

[14] J. G. Pipe, "Motion correction with propeller mri: application to head motion and free-breathing cardiac imaging," *Magnetic Resonance in Medicine: An Official Journal of the International Society for Magnetic Resonance in Medicine*, vol. 42, no. 5, pp. 963–969, 1999.

[15] M. S. Cohen, "Echo-planar imaging (epi) and functional mri," *Functional MRI*, pp. 137–148, 1998.

[16] D. Wang, W. Strugnell, G. Cowin, D. M. Doddrell, and R. Slaughter, "Geometric distortion in clinical mri systems: Part i: evaluation using a 3d phantom," *Magnetic resonance imaging*, vol. 22, no. 9, pp. 1211–1221, 2004.

[17] J. Overweg, "Mri main field magnets," *Phys*, vol. 38, pp. 25–63, 2008.

[18] A. Belov, V. Bushuev, M. Emelianov, V. Eregin, Y. Severgin, S. Sytchevski, and V. Vasiliev, “Passive shimming of the superconducting magnet for mri,” *IEEE transactions on applied superconductivity*, vol. 5, no. 2, pp. 679–681, 1995.

[19] J. Weygand, C. D. Fuller, G. S. Ibbott, A. S. Mohamed, Y. Ding, J. Yang, K.-P. Hwang, and J. Wang, “Spatial precision in magnetic resonance imaging–guided radiation therapy: the role of geometric distortion,” *International Journal of Radiation Oncology* Biology* Physics*, vol. 95, no. 4, pp. 1304–1316, 2016.

[20] “Courtesy of allen d. elster, mriquestions.com.”

[21] F. Schmitt, “The gradient system,” in *Proc. Society of Magnetic Resonance*, 2013.

[22] S. Hidalgo-Tobon, “Theory of gradient coil design methods for magnetic resonance imaging,” *Concepts in Magnetic Resonance Part A*, vol. 36, no. 4, pp. 223–242, 2010.

[23] J. F. Schenck, “The role of magnetic susceptibility in magnetic resonance imaging: Mri magnetic compatibility of the first and second kinds,” *Medical physics*, vol. 23, no. 6, pp. 815–850, 1996.

[24] J. D. Port and M. G. Pomper, “Quantification and minimization of magnetic susceptibility artifacts on gre images,” *Journal of computer assisted tomography*, vol. 24, no. 6, pp. 958–964, 2000.

[25] M. N. Hood, V. B. Ho, J. G. Smirniotopoulos, and J. Szumowski, “Chemical shift: the artifact and clinical tool revisited,” *Radiographics*, vol. 19, no. 2, pp. 357–371, 1999.

[26] P. T. Weavers, S. Tao, J. D. Trzasko, Y. Shu, E. J. Tryggestad, J. L. Gunter, K. P. McGee, D. V. Litwiller, K.-P. Hwang, and M. A. Bernstein, “Image-based gradient non-linearity characterization to determine higher-order spher-

ical harmonic coefficients for improved spatial position accuracy in magnetic resonance imaging," *Magnetic resonance imaging*, vol. 38, pp. 54–62, 2017.

[27] L. N. Baldwin, K. Wachowicz, S. D. Thomas, R. Rivest, and B. G. Fallone, "Characterization, prediction, and correction of geometric distortion in mr images," *Medical physics*, vol. 34, no. 2, pp. 388–399, 2007.

[28] T. M. Seibert, N. S. White, G.-Y. Kim, V. Moiseenko, C. R. McDonald, N. Farid, H. Bartsch, J. Kuperman, R. Karunamuni, D. Marshall, *et al.*, "Distortion inherent to magnetic resonance imaging can lead to geometric miss in radiosurgery planning," *Practical radiation oncology*, vol. 6, no. 6, pp. e319–e328, 2016.

[29] *PolyJet 3D Printers Systems and Materials*, Stratasys, Ltd. 2018.

[30] *Biocompatible Clear MED610*, Stratasys, Ltd. 2018.

[31] Marten, "Stl lattice generator, matlab central file exchange, https://www.mathworks.com/matlabcentral/fileexchange/48373-stl-lattice-generator," retrieved July 22, 2020.

[32] S. Ziegler, H. Braun, P. Ritt, C. Hocke, T. Kuwert, and H. H. Quick, "Systematic evaluation of phantom fluids for simultaneous pet/mr hybrid imaging," *Journal of Nuclear Medicine*, vol. 54, no. 8, pp. 1464–1471, 2013.

[33] ACR, "Phantom test guidance for use of the large mri phantom for the acr mri accreditation program," 2019.

[34] J. B. A. H. D. R. Nina Niebuhr, Martin Requardt, *MRI Geometric Distortion QA using the ACR MRI Accreditation Phantom.* Siemens healthcare, 2014.

[35] CIRS, "Distortion check software for evaluation of image distortion: user guide," 2018.